



Science Arts & Métiers (SAM)

is an open access repository that collects the work of Arts et Métiers Institute of Technology researchers and makes it freely available over the web where possible.

This is an author-deposited version published in: <https://sam.ensam.eu>
Handle ID: <http://hdl.handle.net/10985/24829>

To cite this version :

Corentin POISSENOT, Bertrand MARCON, Bruno BERTHEL, FREDERIC ROSSI, Guillaume FROMENTIN - In situ thermomechanical analysis of the primary shear zone in Inconel 718 orthogonal cutting - The International Journal of Advanced Manufacturing Technology - 2024

Any correspondence concerning this service should be sent to the repository

Administrator : scienceouverte@ensam.eu



In situ thermomechanical analysis of the primary shear zone in Inconel 718 orthogonal cutting

Corentin Poissenot-Arrigoni¹ · Bertrand Marcon¹ · Bruno Berthel² · Frédéric Rossi¹ · Guillaume Fromentin¹

Abstract

Inconel 718 is a challenging alloy to machine, commonly employed in the aeronautic and energy industries. There is a continual need to enhance our understanding of its cutting processes to improve its machining applications. This research presents an in situ analysis of the kinematic and thermal fields behaviour of a serrated chip, during orthogonal cutting in the primary shear zone. This study involves a specific self-designed optical system enabling the simultaneous acquisition of both a visible high-speed CCD camera and an infrared camera via a single $\times 25$ magnification reflective objective. A particular attention is brought to evaluate the accuracy of the whole optical system to measure the thermomechanical fields in the unfavourable peculiar cutting conditions among such are high strain rates, texture evolution, strong thermal gradients, and very narrow observation window. The description of the digital image correlation technic within the visible range and the infrared images post-processing are both affronted, and their limitations exposed. To conclude, a deeper characterisation of the primary shear zone shape is done from the kinematic and the thermal point of views showing that, at least under the employed cutting conditions and for Inconel 718 alloy, the primary shear zone width exhibits no thickness despite the literature.

Keywords Orthogonal cutting · In situ analysis · Full field measurements · Infrared thermography · Digital images correlation · Primary shear zone

1 Introduction

Machining is a material removal process commonly used in industry because it allows obtaining complex shapes on hard material. However, this cutting process implies intricate mechanisms that could undergo severe thermomechanical stress on the machined material, that potentially affects the geometry and the surface integrity of the final part if inadequate cutting conditions are selected [1–3]. Then, the understanding of cutting phenomenon seems to be relevant to predict the impact of the process on the final part.

To experimentally study the thermomechanical loads induced by machining operation, the post-mortem analysis of the chip morphology during a quick stop test could be used [4]. This method gives the orientation of the primary

shear band and information about the maximal stress and the temperature the material underwent through, thanks to the observation of the chip and the subsurface microstructure. To obtain in situ real time information, dynamometer and thermocouples are mainly used to respectively measure cutting force and temperatures [5]. Although these two means of measurement have a high acquisition rate, the dynamometer give only global cutting force and the measures are largely disrupted by the natural frequency and undesirable dynamic influences; whereas thermocouples give only local information and large strain could break down the measures [6]. Therefore, in case of serrated chip formation, it seems very hard to obtain accurate information in the Primary Shear Zone (PSZ).

More recently, full field measurement technics have allowed observing cutting in real time. Trough visible camera and Digital Images Correlation (DIC) analysis, it is possible to have access at the kinematic fields [7], and on another hand, infrared cameras permit the access to the thermal field [8]. In most machining study, only one type of camera is used, however, some contributions have successfully coupled infrared and visible cameras during orthogonal

✉ Corentin Poissenot-Arrigoni
corentin.poissenot@ensam.eu

¹ Arts et Metiers Institute of Technology, LaBoMaP, UBFC, HESAM, 71250 Cluny, France

² Ecole Centrale de Lyon, LTDS, UMR CNRS 5513, Université de Lyon, 69134 Ecully, France

cutting operation [9–13]. In addition, some studies have also coupled visible and infrared cameras too, on other mechanical experiments, as tensile or Hopkinson test [14–19]. In case of machining, it seems that the VISIR developed by Harzallah [11] appears to be up to now the most efficient thermomechanical observation system. However, the infrared camera frame rate and the selected objective seems not optimised to characterize the PSZ.

In the literature, the thermomechanical behaviour under cutting conditions leading to a continuous chip has been largely studied. Thus, it exists several more or less complex formulas to describe the PSZ, validated via experimental results or numerical simulation on specific material and cutting conditions. The contributions of [20] or [21] are ones of the most famous analytical models. However, in the case of serrated chip morphology, there is no analytical solution or numerical model validated in the general case and the complexes mechanisms of the chip formation is not completely understood.

In this study, a new optical system allowing observing simultaneously the kinematic and the thermal in-plane fields is developed. Later, an analysis allowing characterizing the primary shear zone of a serrated chip formation, but being extendable to continuous chip morphology is done.

2 Experimental setup

2.1 Imaging system

To observe the kinematic and the thermal fields during orthogonal cutting, a specific optical system has been designed. The overall optical coupling system is presented on the Fig. 1. Thanks to the proposed imaging system, a

visible camera together with an infrared one can simultaneously record frames through a unique objective. In first, a $\times 25$ reflective objective infinity corrected, with a protected silver coating has been selected, because it operates on a large spectral range including these of the two cameras. The working distance of the objective is 12.5 mm and the depth of field is around the micrometre. Then, a platinum dichroic beam splitter separates the optical flux by wavelengths toward the adequate camera. At the exit of this component, a first optical path is dedicated to the visible camera and a second to the infrared camera. The infrared flux is focused on the sensor thanks to an off-axis parabolic mirror, whereas the visible beam is focused on the visible camera sensor by the means of a tube lens. In addition, on the visible optical path, a beam splitter (50/50; Transmission/Reflection) has been added, in view to embed confocal illumination.

The thermal images are recorded by a Telops MS-M3k camera. This infrared camera has an InSb (Indium Antimonide) sensor operating within the spectral range of 1.50 to 5.50 μm , with a resolution of $320 \times 256 \text{ pixel}^2$, a pitch of 30 μm , and an indicated Noise Equivalent Temperature Difference (NETD) of 25 mK. For this study, a broadband filter with a spectral range of 3.11 to 5.50 μm has been used. For the visible images, a high-speed CCD camera Photron FASTCAM SA-Z has been used. This camera has a sensor resolution of $1024 \times 1024 \text{ pixel}^2$ and a pitch of 20 μm . Table 1 summarizes the main characteristics of the two cameras.

To analyze the images of the two cameras, the synchronization of these two means of measurement has to be insured. Thereby, thanks to a specific trigger and cameras settings, the two means of measurement are synchronized at the nearest of the microsecond. Given the setting, integration time of cameras will be greater than 13 μs , the synchronization is considered as suitable. At the end, the Fig. 2 gives an

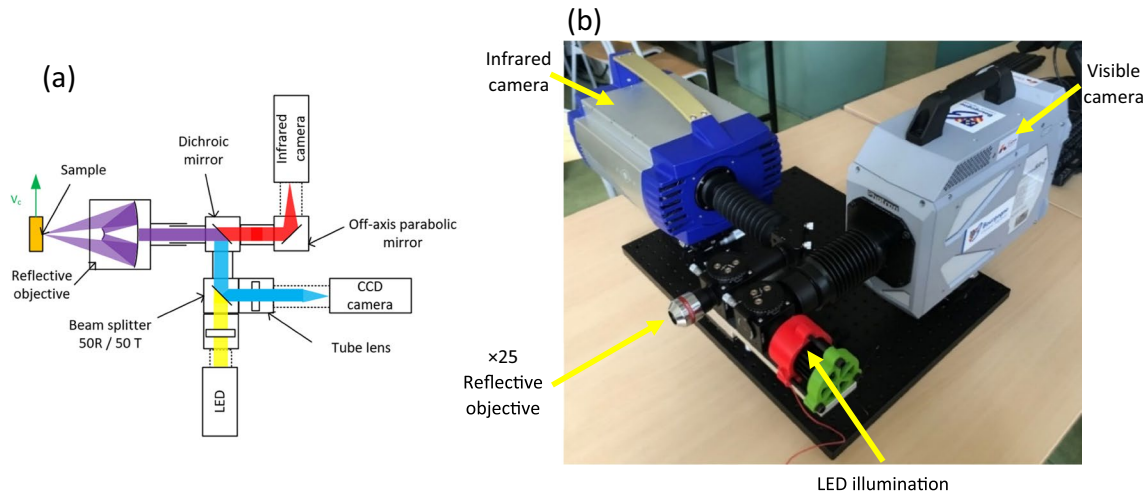


Fig. 1 Presentation of the imaging system: scheme of the optical components (a), view of the system (b)

Table 1 Cameras and frames characteristics

Camera	Telops MS-M3k	Photron FASTCAM SA-Z
Sensor	InSb	CMOS
Spectral range	3.11 – 5.50 μm	0.4 – 1.0 μm
Resolution	320 \times 256 pixel ²	1 024 \times 1 024 pixel ²
Pitch	30 μm	20 μm
Spatial resolution with a $\times 25$ objective	1.25 $\mu\text{m}.\text{pixel}^{-1}$	0.81 $\mu\text{m}.\text{pixel}^{-1}$
Maximum acquisition frame rate	3 100 Hz (image size of 320 \times 256) 100 000 Hz (image size of 64 \times 4)	20 000 Hz (image size of 320 \times 256) 2 100 000 Hz (image size of 64 \times 4)
Setting integration time	1—200 μs	1—1 000 μs

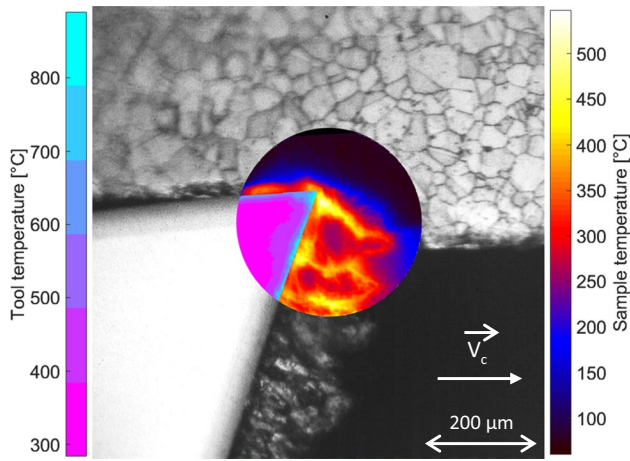


Fig. 2 Example of image obtained via the optical system during orthogonal cutting at $V_c = 4 \text{ m}.\text{min}^{-1}$; $h_{TC} = 0.1 \text{ mm}$ and a rake angle of 20°

example of one combined image obtained via the optical system developed where the thermal field is represented over the observation of the scene at the tip of the cutting tool.

2.2 Orthogonal cutting setup

The orthogonal cutting tests are performed during a planing operation along the x-axis of a DMG DMC 85VL 3-axis gantry milling center embedded with linear motors allowing for rather fast cutting speed ($120 \text{ m}.\text{min}^{-1}$ in the X-direction). In view to facilitate the observation of the serrated chip formation, the sample is embedded on the X-axis carriage thanks to a specific part-clamping device (sample moves) and the tool is clamped on the machine table (tool is fixed). Concerning the frames acquisition, the thermomechanical observation system is placed in front of the tool. Figure 3 shows the orthogonal cutting experimental design.

A 2 mm thick (Y-direction) and 30 mm in length (X-direction) sample in Inconel 718 has been machined. This super alloy used in aeronautic industry has been selected because its low thermal conductivity induces a

high temperature in the primary shear zone and a serrated chip could be formed even at low cutting speed. Therefore, the serrated chip formation process may be observed with a low acquisition frame rate, then compatible with the limitations of the infrared camera (frame rate and integration time). For this study, an uncoated carbide tool with a rake angle of 20° and a cutting-edge inclination of 1.68° (measured once the tool is clamped in the machine) have been selected. Although the geometry of this tool is not optimised to machine nickel-based alloy, it has been chosen because its significant rake angle ($\alpha = 20^\circ$) allows limiting the lateral burr and the lateral expansion of the chip, whom could lead to blurred images due to the low depth of field of about 1 μm of the $\times 25$ reflective objective. In addition, the non-zero cutting-edge angle is necessary to bring the side burr and out of plane deformations as much as possible toward the opposite of the observed surface. To finish, Table 2 presents cutting conditions and cameras setting used for each pass.

2.3 Images characterisation and processing

Given that cameras are used, the observed surface preparation of the samples could have a significant influence on the quality of the recorded experimental data, either within the visible range for the displacement fields from DIC analysis (inhomogeneous surface pattern, correlation error, etc.), and within the infrared range (emissivity, reflections, etc.). It is well-known that for digital images correlation, a randomly textured surface is the optimum, whereas a mat homogeneous surface with as high as possible emissivity is recommended for the infrared thermography. Therefore, to perform the two technics simultaneously, a trade-off must be found. Therefore, the sample is polished and etched by Adler solution to create a speckle pattern for the DIC purpose, and a thin carbon coating is added to raise the emissivity of the observed scene by darkening the surface and being enough transparent to keep the Inconel microstructure (emphasized by the Adler chemical attack) exploitable by the DIC software.

A defect in optical component or in the mirror alignment could lead to distortions along both optical paths. The magnification assessment has been conducted through two different methods: by DIC and with the observation of calibrated indentations prints (obtained by Knoop and Vickers tests). According to Table 3, the spatial resolution of the

visible path is $0.81 \mu\text{m}.\text{pixel}^{-1}$ and $1.25 \mu\text{m}.\text{pixel}^{-1}$ for the infrared path.

Based on [22], an integration time insensitive and pixel wise radiometric calibration has been implemented. A CI System SR-800R-7A-ET-HU black body source has been used to obtain the experimental data required to implement

Fig. 3 Orthogonal cutting configuration in the machine tool

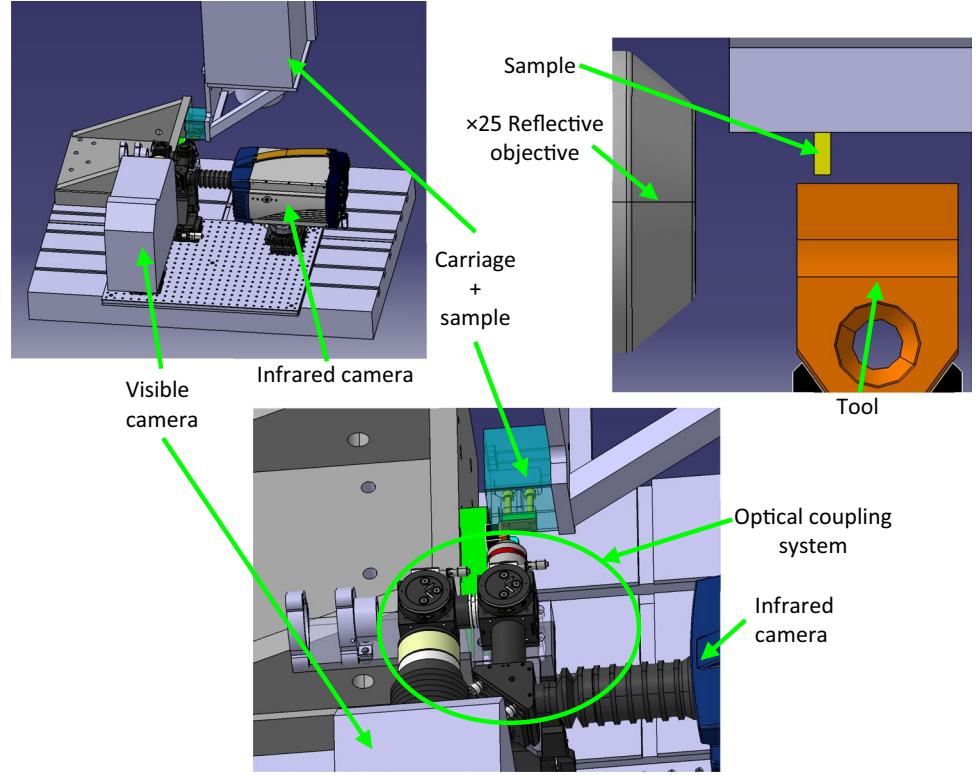


Table 2 Camera settings (f_{acq} : frame acquisition rate, IT: Integration Time) in correspondence to cutting conditions used in this study (h_{TC} : cut thickness, V_c : cutting speed)

Test	Cutting conditions		Infrared camera setting			Visible camera setting		
	h_{TC} [mm]	V_c [m.min ⁻¹]	Resolution [pixel ²]	f_{acq} [Hz]	IT [μs]	Resolution [pixel ²]	f_{acq} [Hz]	IT [μs]
1	0.1	4	192 × 132	4 000	90	1 024 × 1 024	20 000	35.00
2	0.1	10	192 × 132	6 000	37	1 024 × 688	30 000	26.25
3	0.1	15	192 × 132	6 000	27	512 × 512	60 000	15.66
4	0.1	20	192 × 132	6 000	20	512 × 512	60 000	13.75

Table 3 Assessment of the spatial resolution of each optical path

Test	Visible path			Infrared path		
	Test mark size [pixel]	Test mark size [μm]	Spatial resolution [μm.pixel ⁻¹]	Test mark size [pixel]	Test mark size [μm]	Spatial resolution [μm.pixel ⁻¹]
Indentation 1	231	187	0.810	149	187	1.255
Indentation 2	148	120	0.811	96	120	1.250
Indentation 3	79	64	0.810	51	64	1.254
DIC			0.811			1.250

the radiometric calibration, as shown of the Fig. 4(a). According to the Fig. 4 (b), the digital levels fluxes of the infrared camera evolve linearly compared to the radiance of the observed black body source. Then, the calibration curve is a straight line. Therefore, only few experimental points are necessary to create a global calibration on large temperatures range (this point being widely affronted in [22]). Figure 4 (c) presents the assessment of the calibration. Based on more than 1 200 000 measures, this radiometric calibration leads to a mean error of +1.02 °C, a standard deviation of 1.50 °C, and all the values have an error included in the interval [-5.93; +8.28] °C.

According to [23], thanks to the Telops MS-M3k multi-spectral infrared camera mounted with pairs of filters and used as bi-chromatics pyrometer, a mean emissivity (ϵ) of 0.39, with a standard deviation of 0.02 has been measured on the spectral range 3.11–5.50 μm for the observed Inconel 718 sample, as shown on the Fig. 5. Therefore, for the rest of the study, a constant emissivity of 0.39 will be used for the image processing.

The conversion from the radiance to the absolute temperature is possible thanks to equation developed by [24].

$$Rad(Im_{X,Y}) = \epsilon_{\lambda_1, \lambda_2} * \int_{\lambda_1}^{\lambda_2} \frac{2hc^2 \lambda^{-5}}{\exp\left(\frac{hc}{\lambda k T_{Im_{X,Y}}}\right) - 1} d\lambda + (1 - \epsilon_{\lambda_1, \lambda_2}) * \int_{\lambda_1}^{\lambda_2} \frac{2hc^2 \lambda^{-5}}{\exp\left(\frac{hc}{\lambda k T_{env}}\right) - 1} d\lambda$$

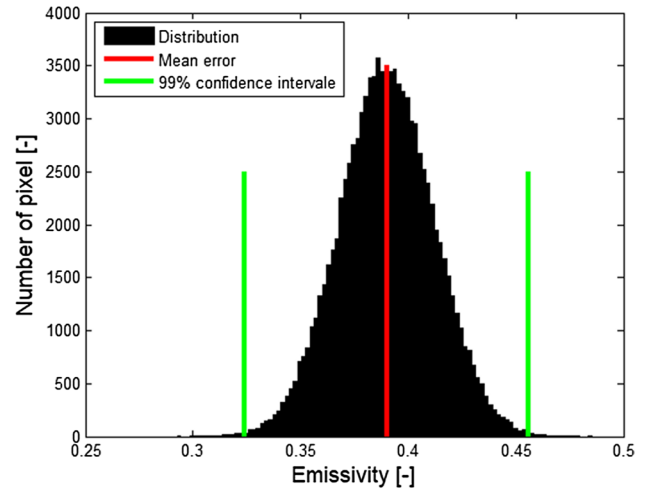
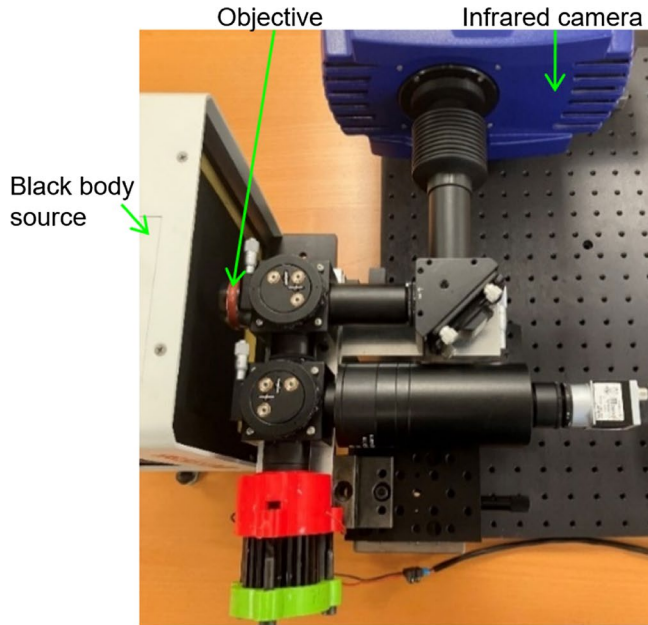


Fig. 5 Distribution of the emissivity of the Inconel 718 sample polished and chemically attacked by Adler solution

with Rad and T , the radiance and the absolute temperature of the pixel with the coordinates X, Y for the image Im , $\epsilon_{\lambda_1, \lambda_2}$ the emissivity of the observed scene, λ_1, λ_2 the spectral range of the infrared camera, h the Planck constant, k the Boltzmann constant, c the celerity of the light, T_{env} the radiometric temperature of the environment. The usual Planck's law expressed for a solid angle not having analytical solution, the integral is calculated numerically by the trapeze method with a step of $3.9 \times 10^{-4} \mu\text{m}$, which discretizes the spectral band in 1000 elements with a considered low residue. The

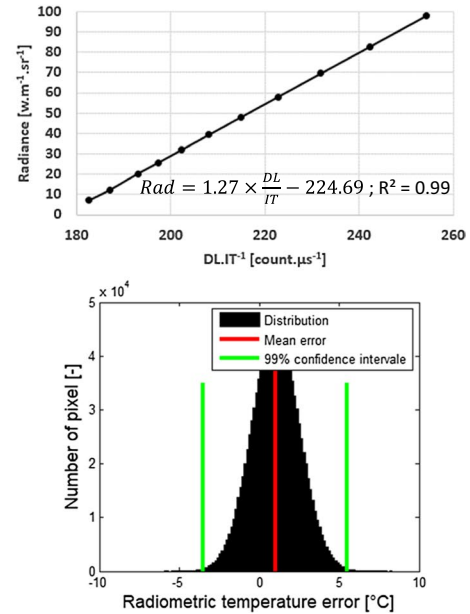


Fig. 4 Radiometric calibration procedure: experimental set up (a), calibration curve (b), and radiometric calibration error (c)

Table 4 Input parameters necessary to convert the radiance of a pixel in absolute temperature

Parameters	Values
Planck constant: h	$6.6226176 \times 10^{-34}$ [J.s]
Boltzmann constant: k	1.380662×10^{-23} [J.K ⁻¹]
Celerity of the light: c	2.998×10^8 [m.s ⁻¹]
Spectral range of the IR camera sensor: λ_1 - λ_2	3.11—5.50 [μ m]
Environment temperature: T_{Env}	20.0 [°C]
Emissivity: ϵ	0.39 ± 0.02 [-]
Wavelength discretization for the Planck's equation integral	3.90×10^{-4} [μ m]
Temperature discretization for Planck's equation integration	0.1 [K]

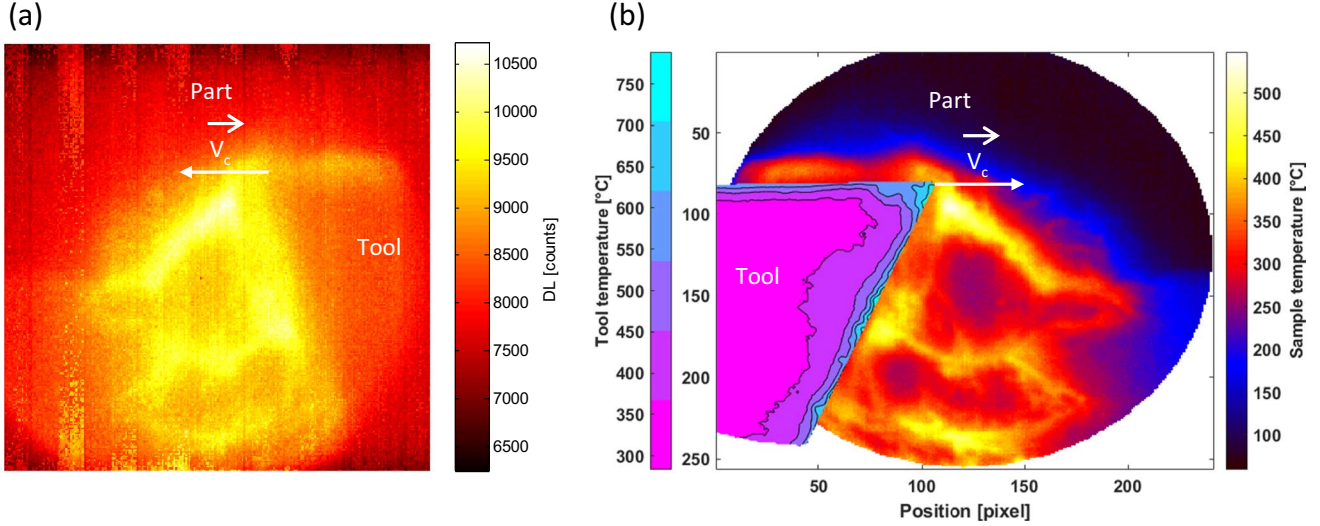


Fig. 6 Example of the thermal image processing of an Inconel 718 orthogonally cut, with $V_c=4$ m.min.⁻¹; $h_{TC}=0.1$ mm: raw data in digital level from the infrared camera sensor (a), absolute temperature post-processed data (b)

Table 4 summarizes parameters uses to convert the digitals levels given by the camera in absolute temperatures.

Finally, Fig. 6 presents a result of the thermal image processing to access the absolute temperature of the observed scene. Beyond the method allows to convert digital levels in absolute temperature, an important numerical processing is applied through the radiometric calibration to homogenize the pixel response and have accurate and reliable thermal data.

The characterization of the kinematic fields in the primary shear zone by the DIC method does not seem trivial. Indeed, the large deformations (both in-plane and out of plane) in this zone can alter the shades of gray levels (DIC being based on the grey level conservation principle) or even make the images blurry. The strong kinetics observed in this zone can also induce streaking phenomena and therefore blurred images that will have the direct consequence of degrading the uncertainty of DIC measurement. It is thus obvious that in the context of machining, the images obtained are degraded compared to quasi-static mechanical tests. According to Hild and Roux [25], a DIC method based on a global approach seems more efficient to

Table 5 Setting of the Correli Q4 software for the DIC analysis

Zone of Interest (ZOI) size	16 pixels
Number of scales	3
Maximum number of iterations	200
Type of calculations	Incremental DIC calculations

measure complex displacements with noisy reference images compared to a local DIC method. In addition, according to [26–28], a global DIC approach seems to be more adapted than a local method to estimate discontinuous deformation. Therefore, the Correli Q4 software [29], which is based on a global approach, is selected. Table 5 summarizes the configuration of this DIC software, according to [29], and the results of the pre-analysis modules available in the software to minimize the correlation errors by selecting the best discretization size, called zone of interest (ZOI), number of scales, and the number of iterations to reach a satisfying convergence of the calculation.

To characterize the DIC performance and optical distortions, a pass with the correct cutting speed but without machining is performed (only sample translation) and a DIC calculus has been realized. As shown on Fig. 7, after removing the rigid body motion, a standard deviation of 0.23 pixel (corresponding to $0.18 \mu\text{m}$) is obtained for the total displacement and all the results are included in the interval $[-0.9; 0.8]$ pixel (corresponding to $[-0.73; 0.65] \mu\text{m}$). Therefore, in the rest of the study it will be considered that all DIC results are included within the range of $[-0.73; 0.65] \mu\text{m}$. These results show a drawback in alignment of the optical components since the errors are spread uniformly over the observed surface.

In the end, thanks to a camera coupling system, a milling operation was instrumented, making it possible to simultaneously observe the kinematic and the thermal fields under cutting conditions.

3 Results and discussion

3.1 Analysis of the strain in the primary shear zone

To study the mechanical characteristics of the primary shear zone, DIC analysis is performed. Firstly, to define the localization of the strain, a mean of the equivalent Von Mises strain, based on the analysis of 1200 consecutive images (corresponding approximately to the creation of 25 segments), after the cutting stabilized has been calculated (far from the tool entrance into the work material and far from its exit). In addition, the limits of the deformed area have been defined, as shown on the Fig. 8 (red lines). It is important to

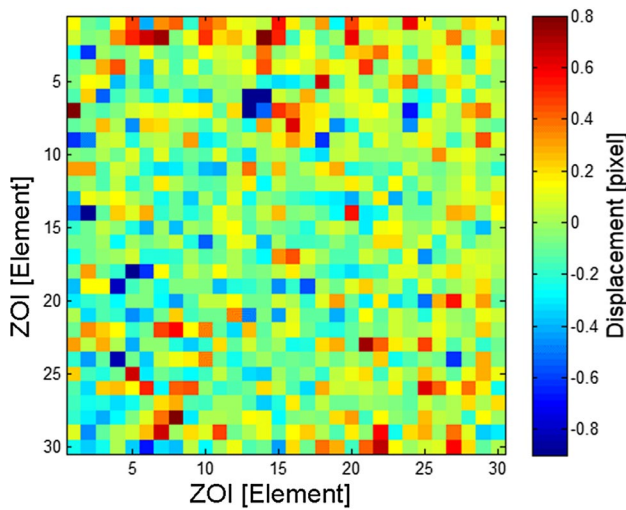


Fig. 7 Assessment of the DIC calculation errors by ZOI over the observed Inconel 718 sample surface (polished, Adler chemical attack, no machining, and $V_c = 20 \text{ m.min}^{-1}$), 1 ZOI = 16 pixels

note that the absolute strain values depend on the acquisition frame rate of the visible camera, because incremental DIC has been used. However, the use of incremental DIC has no impact on the localization of the deformed region.

According to the Fig. 8, it seems that the deformed region may be likened to an oval shape, rather than a band. To complete the analysis, the mean width and length of the deformed zone has been estimated at respectively 42 and $249 \mu\text{m}$. By using the same method, the analysis of the deformed region has been conducted for others cutting conditions. The results are synthetized in Table 6.

According to Table 6, it seems that the cutting speed has no significant influence on the size of the deformed shape localized close to the primary shear zone, which agrees with the literature.

As mentioned before, these first results are based on the formation of several segments (25). Then, it is not really possible to define at each instant the characteristics of the primary shear zone. To define more accurately the mechanical aspect of this specific region, the analysis of the formation of one segment (that represents approximately 50 consecutive images for a cutting speed of 4 m.min^{-1}) has been done. For this, for each image, the center of the primary shear zone is

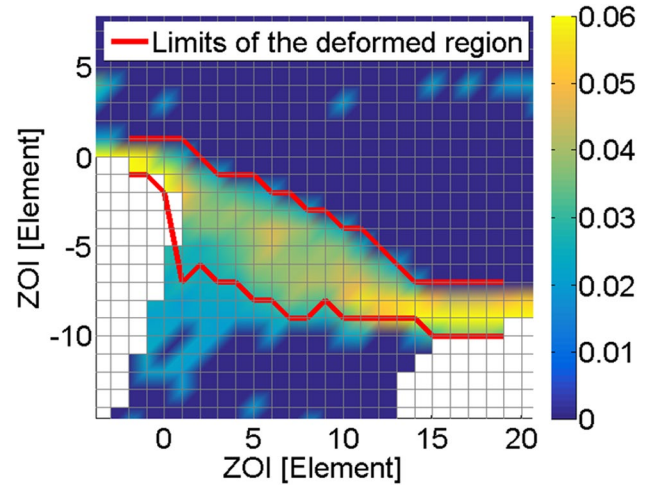


Fig. 8 Localization of the deformed area with the mean of the equivalent Von Mises strain at $V_c = 4 \text{ m.min}^{-1}$; $h_{TC} = 0.1 \text{ mm}$

Table 6 Characteristics of the primary shear zone for different cutting conditions

Cutting conditions		Deformed zone characteristics	
$V_c [\text{m.min}^{-1}]$	$h_{TC} [\text{mm}]$	Width $[\mu\text{m}]$	Length $[\mu\text{m}]$
4	0.1	42	249
10	0.1	38	245
15	0.1	46	247
20	0.1	40	248

determined by assuming that its center is localized where the largest strain is observed. Table 7 shows the reference image and the DIC results with the center of the PSZ, plotted arbitrarily for 5 different images along the formation of one segment. In addition, on the Fig. 9, the curves of the centers of the primary shear zone of each image presented in Table 7, are plotted on the same graphic, in order to track the evolution of the localization of the primary shear zone at different instants of the segment formation.

Firstly, according to the Fig. 9, it seems that the center of the primary shear zone is not fixed over time and its shape evolves with different forms of curves. At the start of the

segment creation (image 1), the center of the primary shear zone looks like a convex curve, then at the middle (image 117), it fits to a straight line and to finish (image 150), it seems to be similar with a concave curve. These different shapes of the primary shear zone could be explained by the fact that the non-deformed material moves at the imposed cutting speed, and then, the deformed material is pressed by the flow of the undeformed material. At the end, it seems that the localization of the primary shear zone is not fixed during the process of the segment formation.

Secondly, based on each DIC results presented in the Fig. 10, it seems that the width of the PSZ is approximately

Table 7 DIC results at different instants of a segment formation ($V_c=4 \text{ m.min}^{-1}$; $h_{TC}=0.1 \text{ mm}$)

	Reference image	Deformed image
Image 01		
Image 11		
Image 17		
Image 32		
Image 50		

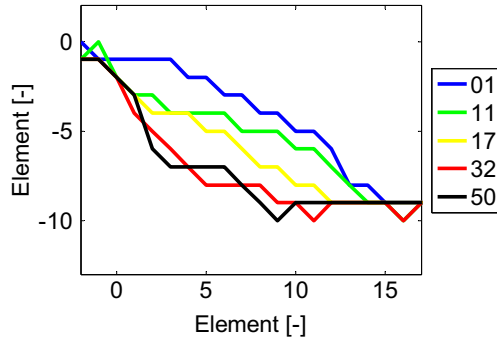


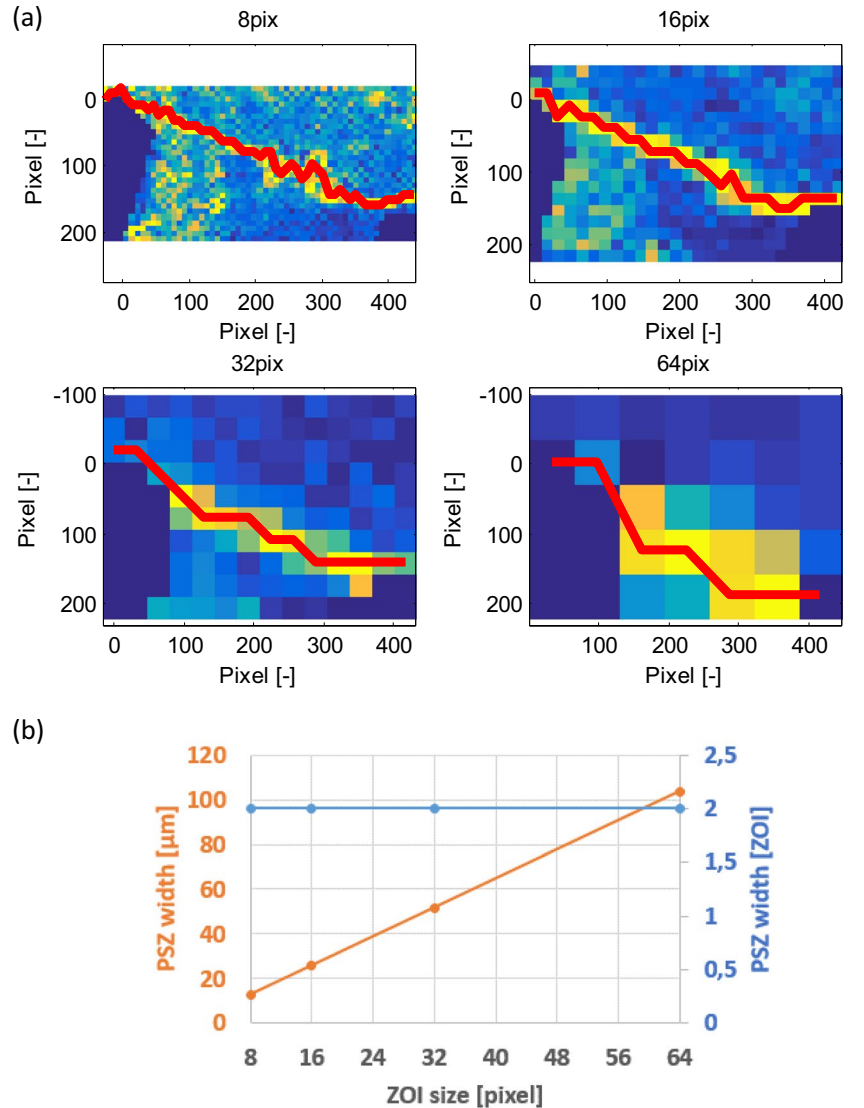
Fig. 9 Analysis of the formation of a segment ($V_c=4 \text{ m.min}^{-1}$; $h_{TC}=0.1 \text{ mm}$)

of 2 ZOIs (with a ZOI size of 16 pixels). However, all the DIC calculations have been realized with the same ZOI size and the mesh is not aligned with the strain, then it seems

not possible to conclude about the width of this region, with these results. It is accepted by the community that the PSZ has a so-called width, as in Grezik's [30] geometrical model for example. Nevertheless, it seems not that obvious when looking at the PSZ with sufficient magnification. To try to define correctly a PSZ width, DIC computation is performed on the same reference and deformed images (respectively images number 11 and 12) varying only the ZOI size from 8 to 64 pixels as represented in the Fig. 10.

As shown in Fig. 10(b), the deformed width and then the potential PSZ width, is constant with a value of 2 ZOIs, no matter the size of the ZOI. Then, via the application of the spatial resolution, this parameter value would rise depending on the ZOI size, that it seems not reasonable. Thus, it seems that the DIC method, with ZOI sizes used in this study (8 pixels or higher) is not able to accurately characterize the PSZ width. Therefore, in these specific experimental conditions (sample in Inconel 718; $V_c=4 \text{ m.min}^{-1}$; $h_{TC}=0.1 \text{ mm}$),

Fig. 10 Description of the PSZ width for different ZOI sizes from 8 to 64 pixels: DIC results (a), PSZ width according to DIC results (b)



if the PSZ has any dimension, is for sure at least lower than $12.96\text{ }\mu\text{m}$ (result obtained for a ZOI of 8 pixels). In addition, based on these results and the videos recorded during orthogonal cutting, where it is possible to see a slipping during the formation of a segment, it could be possible to consider that the PSZ is the result of the slipping of two surface and then it has no width. However, the results presented in this study do not allow validating or refuting definitely this hypothesis.

At the end, it seems that in these experimental conditions, leading to the formation of serrated chip, the strain in the primary shear zone evolves in a deformed oval-shaped region with time. In addition, at a specific instant, the shape of the primary shear zone is not necessarily a straight line, but a convex or a concave curve depending on the progress in the process of the serrated chip formation. To finish, the elements of this study do not allow concluding about a primary shear zone width and suggesting that it has no width, because it could result in a slipping of two surface.

3.2 Thermal characteristics in the primary shear zone

To extend that the analysis of strain via the DIC method did not allow to define clearly the characteristics of the primary shear zone, it has been decided to try to improve its understanding using thermal field data. However, the infrared camera does not offer a high acquisition frame rate like the visible camera. Therefore, to have the most images possible during the creation of one segment, the data from the test with a cutting speed of $4\text{ m}\cdot\text{min}^{-1}$ have been exploited.

Table 8 presents the thermal field of the primary shear zone during the formation of one segment. Firstly, according to the image 1, it seems that the heat source starts close to the tool tip, and then, based on image 2 to 4, it spreads toward the free side of the chip. To extend that, the tool tip is a region with a large compression strain that could be the initiation mechanism of the segment and hence constitutes an important heat source. These observations are corroborated by [31], which observed the same mechanism initiating the formation of a segment (from the tool tip, to the free edge of the chip) in a Ti6Al4V, using a visible camera.

To try to establish the thermal characteristics of the PSZ, the center of this region has been defined once again in the same way than for the DIC analysis (previous subsection), by considering that the center of this zone is localized where the temperature reaches its maximum (as shown in example on the Fig. 11 (a)). Next, a straight-line perpendicular to the center of the primary shear zone is traced and for each pixel of this straight line, the mean temperature parallel to the primary shear zone is calculated. As a result, for each image, a profile curve of the temperature is obtained, as presented on the Fig. 11(b).

On this profile curve, from pixels 150 to 67, corresponding to the pixels in the work part, a rise of the temperatures

is observed. Then, at the pixel 66, the maximum temperature corresponding at the center of the thermal primary shear zone is observed. To finish, from pixels 65 to 1, the cooling in the chip is observed. Based on this profile curve, it seems not trivial to define clearly a width of the primary shear zone, because the diffusivity of the heat in the material, induces continuous smooth temperatures, not allowing identifying singular points considered than boundaries of the primary shear zone. A criterion based on temperature gradient cut-off could be established, however, the elements of this study are unclear from determined an objective cut-off value.

By plotting temperatures profiles for different images, it is possible to obtain the temperature evolution during the formation and development of a single segment, as shown on the Fig. 12.

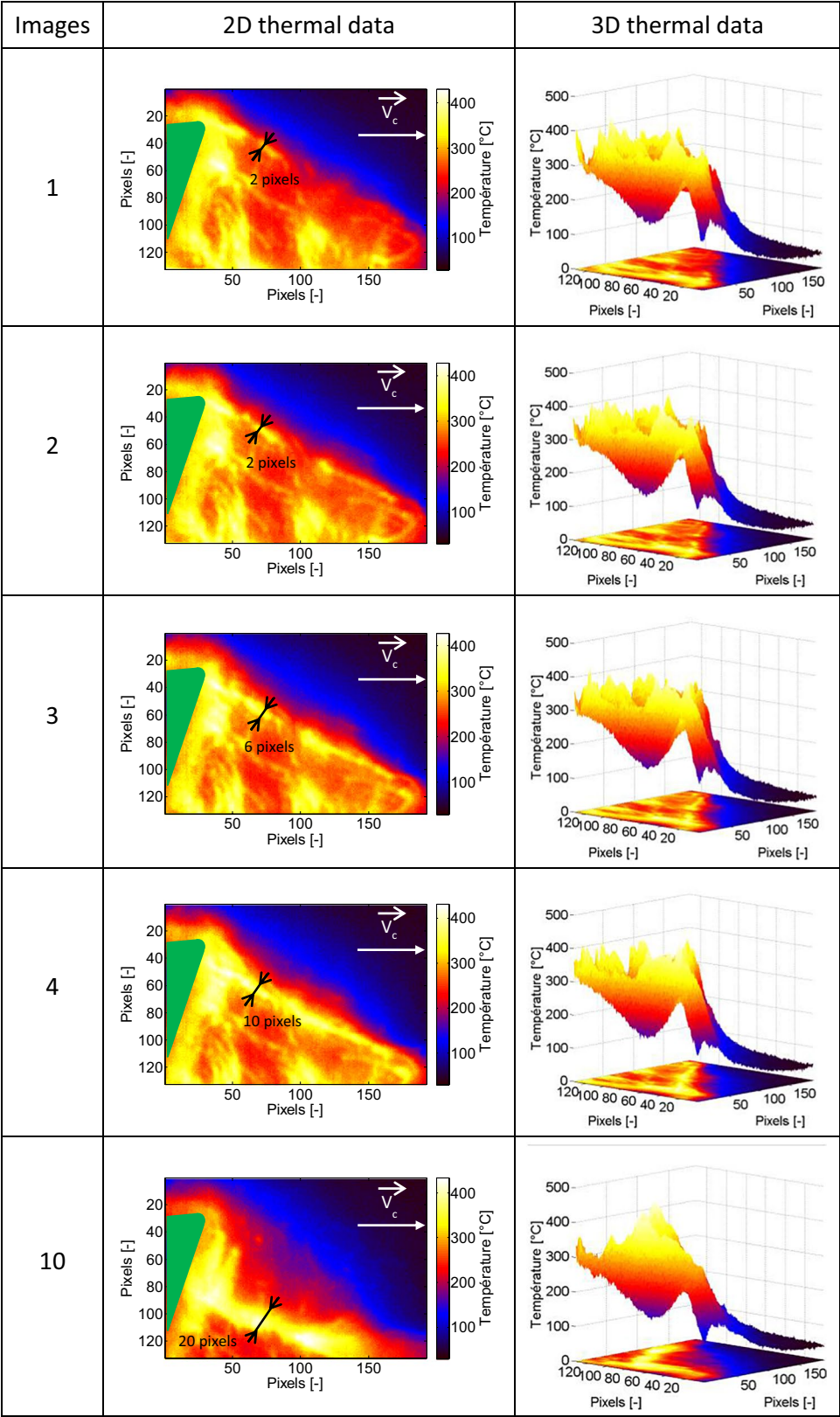
According to the Fig. 12(b), it seems that the width of the hot region increases with time. In fact, it is possible to see that the portion of material with a temperature upper than $350\text{ }^{\circ}\text{C}$ (corresponding to colors yellow and white on the Fig. 12), is empty at the image 1 and higher than 20 pixels at the image 15. To complete this observation, the width of the hot temperature region has been estimated directly on each image, as shown on the Table 8. The estimated width started with a size of 2 pixels at the image 1 and finished with a size of 20 pixels at image 10. Thus, the width of the hot region expands with the progress of the creation of the segment. However, the size of the hot region does not necessarily correspond to the size of the heat source, because via the diffusivity of the material, the heat is conducted into the sample. In addition, given that for images 1 and 2, the width of the measured heat source is 2 pixels, it is conceivable that the means of measurement is not able to characterize this size. It is just possible to say, as previously, that at the initiation of the segment, the width of the heat source in the primary shear zone has a size equal or inferior at 2 pixels, corresponding to $2.50\text{ }\mu\text{m}$.

According to the Fig. 12(a), it seems that from images 1 to 6, the temperature in the center of primary shear zone (corresponding to the pic of temperature) rises at each image, and then, from images 7 to 15, the temperature is relatively constant. The rise in temperature may be explained by a heat source caused by material deformation, and after, the maximum temperature stops rising because there is no more heat source. However, to confirm or refute this hypothesis, a simultaneous analysis of kinematic and thermal field should be done.

3.3 Comparison between strain and temperature fields and interest of the coupled system

As a reminder, both cameras observe through a single lens, thanks to the developed optical system. Additionally, in this study, particular attention has been given to the synchronization of measurement means. It has been demonstrated

Table 8 Absolute temperature (with $\varepsilon=0.39$) in the primary shear zone during the formation of a segment ($V_c=4\text{ m.min}^{-1}$; $h_{TC}=0.1\text{ mm}$)



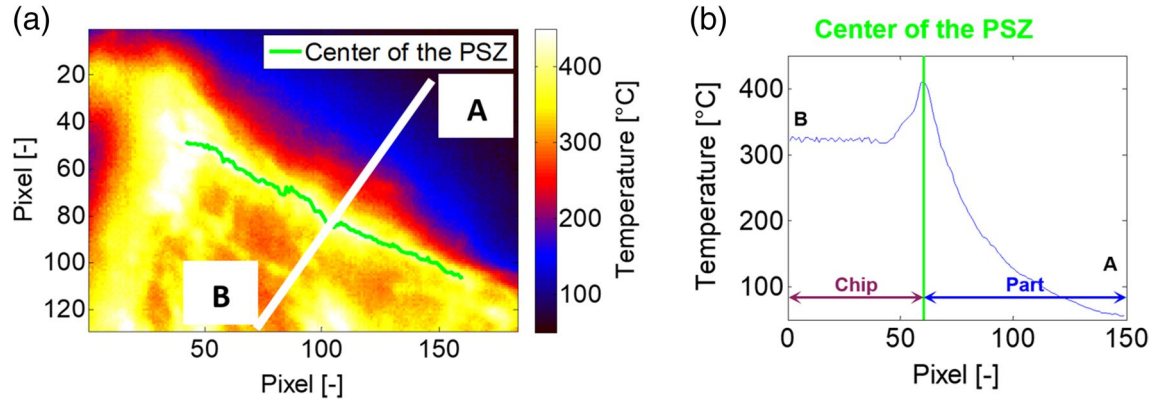


Fig. 11 Definition of the center of the PSZ and this perpendicular straight line, mean temperature perpendicular to the primary shear zone for the image 4

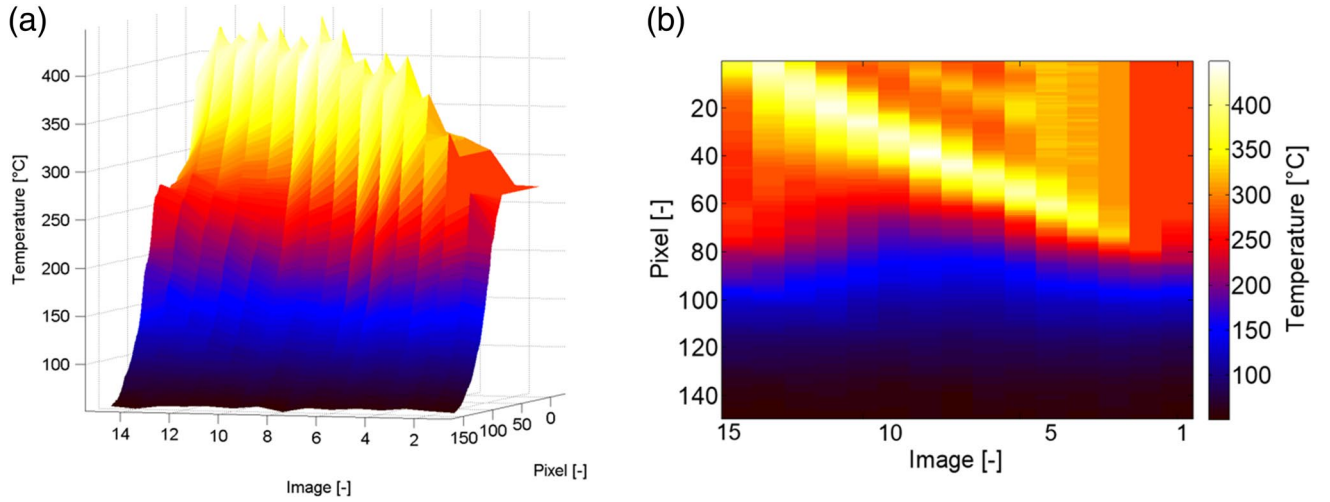


Fig. 12 Monitoring of the creation and development of a single segment over time

that the cameras' synchronization error is less than a micro-second. Consequently, as the thermal and visible cameras observe the same scene at the same moment, it is possible to conduct simultaneous analyses of both the kinematic and thermal fields.

In accordance with the Fig. 13, depicting the evolution of average deformations and temperatures in the primary shear zone during the creation of a segment, it can be observed that the onset and rise in deformation are sudden, while the temperature increase is rather slow and smoothed. Moreover, there is a temporal delay in the temperature rise compared to deformations. To finish, in theory, the temperature curve should descend after a certain time; however, this observation could not be made, because the field of view of the infrared camera is too small to observe the phenomenon.

The observed temporal delay in the thermal field compared to the strains can be explained by several hypotheses.

Firstly, the camera observes the lateral face of the specimen, which is directly subjected to convection with the air. It is therefore not certain that this delay is present at the center of the specimen. It has been shown in the literature by [6, 32, 33] that the center of the specimen is hotter than its lateral faces for a continuous chip in a steady-state, but no study has focused on the temporal evolution of temperature in the depth of the specimen. Secondly, in this study, it was assumed that the emissivity is constant for thermal data post-processing. However, the temperature increase could lead to chip oxidation and, consequently, an undesired increase in emissivity (resulting in higher absolute temperature assessment than actual ones since a lower and homogeneous emissivity is assumed). In practice, the measured temperatures are below the characteristic oxidation temperatures of Inconel 718 (around 600 °C), and no visual oxidation has been observed on the chip. However,

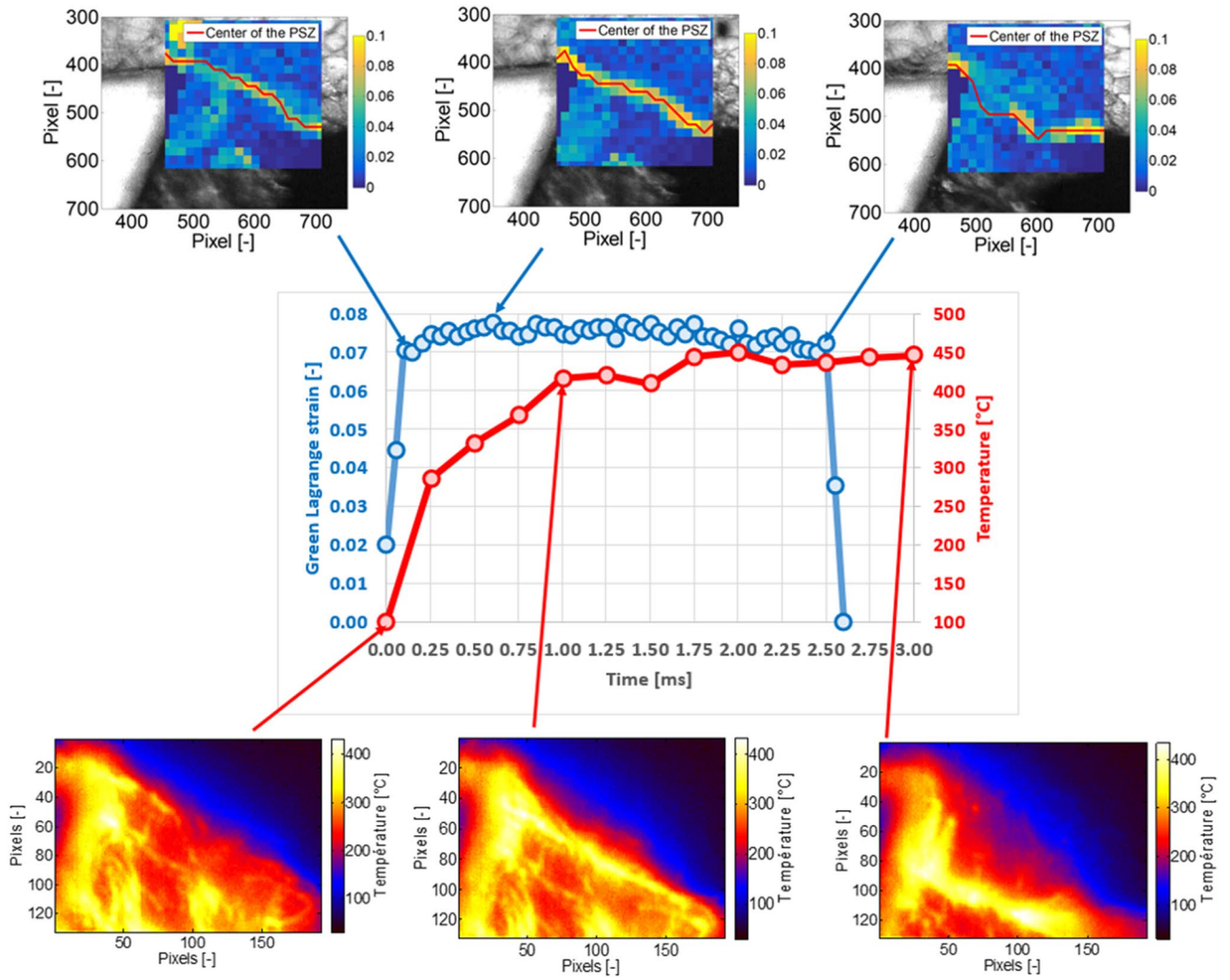


Fig. 13 Evolution of the strain and the temperature in the PSZ toward the time, with $V_c = 4 \text{ min.min}^{-1}$; $h_{TC} = 4 \text{ m.min}^{-1}$

this visual inspection does not exclude a local change in emissivity at the micron scale, which is the order of magnitude of the spatial resolution of the camera. Lastly, material diffusivity phenomena could partly influence the average temperature and thus be a source of temporal shift in the observed temperature on the lateral face of the specimen. Nevertheless, no data is available about the time needed for the oxidation to take place, the delay of about 1 ms seems rather short and this only reason for the temperature increase cannot explain by itself the whole phenomenon.

To resume, it seems that the strain and the temperature curves could be correlated, although there is a time delay for the thermal curve. However, with the elements of this study, it is not possible to affirm that the heat source is caused by the strain undergoing in the material because the DIC technic as set here, is not able to characterize accurately the width of the primary shear zone and the infrared camera allows just to identify a hot region and not to define heat sources.

4 Conclusion

Thanks to a specific optical system, an orthogonal cutting experiment has been observed simultaneously by a visible and an infrared camera, providing access to the experimental thermomechanical field. Although difficult for carry out, due to its low depth of field, the deployment of a $\times 25$ reflective objective has allowed accurate observations with low spatial resolution.

A DIC analysis of the strain undergoing in the part in the primary shear zone shown that at each instant, the deformed region has a specific shape, from a convex curve at the initiation of the of the process, to the concave curve at the end of the creation of the segment, including a straight line at the middle. A characterization of the kinematic width of the primary shear zone has been attempted, however, in the conditions of this study, the value of this parameter is too low to be determined accurately by the DIC method and the optical system limits. Nevertheless, the analysis tends toward a null PSZ width even

though this statement contradicts the concept of a PSZ width largely expressed in literature. To mitigate this strong comment, one should separate what is usually considered a PSZ width after post-mortem observation (effective deformation of the microstructure around the shearing plan. Therefore, just an upper bound of the width of the primary shear zone has been established. However, based on the analysis of several segment, a deformed region in which the primary shear zone moves at each instant, has been defined. The size of this region being stable in time, a width and a length of this zone could be established for different cutting conditions.

Thanks to the data of the infrared camera, the thermal field has been analysed. According to them, it seems that the heat source starts at the tool tip (or really nearby) and then propagates towards the free edge of the material. As for the mechanical behaviour, attempts to measure the width of the primary shear zone in the thermal field found some limitations. Among them, the continuous temperature due to the diffusivity of the heat in the material did not allows establishing an accurate and objective boundary of this zone. It is suggested that the heat source in the primary shear zone could be the consequence of the material strain. However, the size of the observed phenomena is too low to confirm this hypothesis.

To finish, given neither the infrared camera nor the DIC method is able to defined the width of the primary zone (width of heat source and deformed zone at each instant inferior to 2.5 and 12.96 μm respectively), and according to recording videos, it may be possible to consider that the primary shear zone as no width and results mainly, if not entirely, in a slipping of two surfaces one above the other.

Competing interests The authors declare no competing interests.

References

- Liang X, Liu Z (2017) Experimental investigations on effects of tool flank wear on surface integrity during orthogonal dry cutting of Ti-6Al-4V. *Int J Adv Manuf Technol* 93(5–8):1617–1626. <https://doi.org/10.1007/s00170-017-0654-x>
- Chau SY, To S, Wang H, Yip WS, Chan KC, Cheung CF (2021) Effect of cutting speed on surface integrity and chip formation in micro-cutting of Zr-based bulk metallic glass. *Int J Adv Manuf Technol* 114(11–12):3301–3310. <https://doi.org/10.1007/s00170-021-06863-4>
- Wang B, Liu Z (2018) Influences of tool structure, tool material and tool wear on machined surface integrity during turning and milling of titanium and nickel alloys: a review. *Int J Adv Manuf Technol* 98(5–8):1925–1975. <https://doi.org/10.1007/s00170-018-2314-1>
- M'Saoubi R, Ryde L (2005) Application of the EBSD technique for the characterisation of deformation zones in metal cutting. *Mater Sci Eng A* 405(1–2):339–349. <https://doi.org/10.1016/j.msea.2005.06.002>
- Lazoglu I et al (2017) Thermal analysis in Ti-6Al-4V drilling. *CIRP Ann* 66(1):105–108. <https://doi.org/10.1016/j.cirp.2017.04.020>
- Hamm I, Poulachon G, Rossi F, Biremaux H (2021) Innovative experimental measurements of cutting temperature and thermal partition during Ti-6Al-4V orthogonal cutting. *Procedia CIRP* 102:281–286. <https://doi.org/10.1016/j.procir.2021.09.048>
- Baizeau T, Campocasso S, Fromentin G, Besnard R (2017) Kinematic Field Measurements During Orthogonal Cutting Tests via DIC with Double-frame Camera and Pulsed Laser Lighting. *Exp Mech* 57(4):581–591. <https://doi.org/10.1007/s11340-016-0248-9>
- Outeiro JC, Dias AM, Lebrun JL (2004) Experimental Assessment of Temperature Distribution in Three-Dimensional Cutting Process. *Mach Sci Technol* 8(3):357–376. <https://doi.org/10.1081/MST-200038984>
- Arriola I, Whitenon E, Heigel J, Arrazola PJ (2011) Relationship between machinability index and in-process parameters during orthogonal cutting of steels. *CIRP Ann* 60(1):93–96. <https://doi.org/10.1016/j.cirp.2011.03.082>
- Zhang D, Zhang X-M, Ding H (2016) A study on the orthogonal cutting mechanism based on experimental determined displacement and temperature fields. *Procedia CIRP* 46:35–38. <https://doi.org/10.1016/j.procir.2016.03.176>
- Harzallah M, Pottier T, Gilblas R, Landon Y, Mousseigne M, Senatore J (2018) A coupled in-situ measurement of temperature and kinematic fields in Ti-6Al-4V serrated chip formation at micro-scale. *Int J Mach Tools Manuf* 130–131:20–35. <https://doi.org/10.1016/j.ijmachtools.2018.03.003>
- Bonnet C, Pottier T, Landon Y (2021) Proceedings of the Conference Manufacturing'21. Validation d'un modèle numérique de la coupe oblique du Ti-6Al-4V par mesures de champs thermomécaniques couplées, 10–11 juin 2021, Angers, France [In French]. Available: <https://imt-mines-albi.hal.science/hal-03272497/file/Validation-d-un-modele-numerique-de-la-coupe-oblique-du-Ti-6Al-4V.pdf>
- Bonnet C. (2021) Analyse multi-échelle du chargement thermomécanique induit au cours du perçage du Ti-6Al-4V, PhD Thesis [In French], Ecole nationale des Mines d'Albi-Carmaux, 9 december 2021. Available: <https://www.theses.fr/2021EMAC0021>
- Pieczyska EA, Gadaj SP, Nowacki WK, Tobushi H (2006) Phase-transformation fronts evolution for stress- and strain-controlled tension tests in TiNi shape memory alloy. *Exp Mech* 46(4):531–542. <https://doi.org/10.1007/s11340-006-8351-y>
- Orteu J-J, Rotrou Y, Sentenac T, Robert L (2008) An innovative method for 3-D shape, strain and temperature full-field measurement using a single type of camera: principle and preliminary results. *Exp Mech* 48(2):163–179. <https://doi.org/10.1007/s11340-007-9071-7>
- Charkaluk E, Bodelot L, Sabatier L, Noy PD (2009) Proceedings of the French Congress of Mechanic (CFM). Etude du lien entre champs de déformation et champs de température à l'échelle de la microstructure d'un acier inoxydable 316L, 24–28, Marseille, France [In French]. Available: <https://hal.science/hal-03391456v1/document>
- Louche H, Schlosser P, Favier D, Orgéas L (2012) Heat source processing for localized deformation with non-constant thermal conductivity. Application to Superelastic Tensile Tests of NiTi Shape Memory Alloys. *Exp Mech* 52(9):1313–1328. <https://doi.org/10.1007/s11340-012-9607-3>
- Samaca Martinez JR, Balandraud X, Toussaint E, Le Cam J-B, Bergezan D (2014) Thermomechanical analysis of the crack tip zone in stretched crystallizable natural rubber by using infrared thermography and digital image correlation. *Polymer* 55(24):6345–6353. <https://doi.org/10.1016/j.polymer.2014.10.010>

19. Keyhani A, Yang R, Zhou M (2019) Novel capability for micro-scale in-situ imaging of temperature and deformation fields under dynamic loading. *Exp Mech* 59(5):775–790. <https://doi.org/10.1007/s11340-019-00495-2>
20. Merchant ME (1945) Mechanics of the Metal Cutting Process. I. Orthogonal Cutting and a Type 2 Chip. *J Appl Phys* 16(5):267–275. <https://doi.org/10.1063/1.1707586>
21. Oxley PLB (1988) Modelling machining processes with a view to their optimization and to the adaptive control of metal cutting machine tools. *Robot Comput-Integr Manuf* 4(1–2):103–119. [https://doi.org/10.1016/0736-5845\(88\)90065-8](https://doi.org/10.1016/0736-5845(88)90065-8)
22. Poissenot-Arrigoni C, Marcon B, Rossi F, Fromentin G (2023) Fast and easy radiometric calibration method integration time insensitive for infrared thermography. *Infrared Phys. Technol* 104741. <https://doi.org/10.1016/j.infrared.2023.104741>
23. Poissenot-Arrigoni C, Marcon B, Rossi F, Fromentin G (2023) In-situ pixel-wise emissivity measurement using a multispectral infrared camera. *J Imaging* 9(10):198. <https://doi.org/10.3390/jimaging9100198>
24. Li D, Feng C, Gao S, Daniel K, Chen L (2018) Effect of pyrometer type and wavelength selection on temperature measurement errors for turbine blades. *Infrared Phys Technol* 94:255–262. <https://doi.org/10.1016/j.infrared.2018.09.004>
25. Hild F, Roux S (2012) Comparison of local and global approaches to digital image correlation. *Exp Mech* 52(9):1503–1519. <https://doi.org/10.1007/s11340-012-9603-7>
26. Pan B, Qian K, Xie H, Asundi A (2009) Two-dimensional digital image correlation for in-plane displacement and strain measurement: a review. *Meas Sci Technol* 20(6):062001. <https://doi.org/10.1088/0957-0233/20/6/062001>
27. Wang B, Pan B (2016) Subset-based local vs. finite element-based global digital image correlation: A comparison study. *Theor Appl Mech Lett* 6(5):200–208. <https://doi.org/10.1016/j.taml.2016.08.003>
28. Koyanagi J, Nagayama H, Yoneyama S, Aoki T (2016) Time dependence of mesoscopic strain distribution for triaxial woven carbon-fiber-reinforced polymer under creep loading measured by digital image correlation. *Mech Time-Depend Mater* 20(2):219–232. <https://doi.org/10.1007/s11043-016-9292-1>
29. Hild F, Roux S. Correli Q4: A software for-finite-element-displacement field measurements by digital image correlation', Jan. 2008, Accessed: Oct. 16, 2023. [Online]. Available: https://www.academia.edu/15242381/Correli_Q4_A_software_for_finite_element_displacement_field_measurements_by_digital_image_correlation
30. Grzesik W (2008) Advanced Machining Processes of Metallic Materials: Theory. Elsevier, Modelling and Applications
31. Pottier T, Germain G, Calamaz M, Morel A, Coupard D (2014) Sub-millimeter measurement of finite strains at cutting tool tip vicinity. *Exp Mech* 54(6):1031–1042. <https://doi.org/10.1007/s11340-014-9868-0>
32. Arrazola P-J, Aristimuno P, Soler D, Childs T (2015) Metal cutting experiments and modelling for improved determination of chip/tool contact temperature by infrared thermography. *CIRP Ann* 64(1):57–60. <https://doi.org/10.1016/j.cirp.2015.04.061>
33. Soler D, Childs THC, Arrazola PJ (2015) A note on interpreting tool temperature measurements from thermography. *Mach Sci Technol* 19(1):174–181. <https://doi.org/10.1080/10910344.2014.991027>